Title: Cold induces brain region-selective cell activity-dependent lipid metabolism

Authors: Hyeonyoung Min[1], Yale Y Yang[5], and Yunlei Yang[1,2,3,4*]

Affiliations:

1. Department of Medicine Division of Endocrinology, Albert Einstein College of Medicine, Bronx, NY, 10461, USA
2. Department of Neuroscience, Albert Einstein College of Medicine, Bronx, NY 10461, USA
3. Einstein-Mount Sinai Diabetes Research Center, Albert Einstein College of Medicine, Bronx, NY 10461, USA
4. The Fleischer Institute for Diabetes and Metabolism, Albert Einstein College of Medicine, Bronx, NY 10461, USA
5. Friends Seminary, New York, NY 10003, USA

*Correspondence author:

Yunlei Yang

Department of Medicine Division of Endocrinology

Department of Neuroscience

Albert Einstein College of Medicine

yunlei.yang@einsteinmed.edu

Tel: 718-430-8570

Abstract

It has been well documented that cold is an enhancer of lipid metabolism in peripheral tissues, yet its effect on central nervous system lipid dynamics is underexplored. It is well recognized that cold acclimations enhance adipocyte functions, including white adipose tissue (WAT) lipid lipolysis and beiging, and brown adipose tissue (BAT) thermogenesis in mammals. However, it remains unclear whether and how lipid metabolism in the brain is also under the control of cold acclimations. Here, we show that cold exposure predominantly increases the expressions of the lipid lipolysis genes and proteins within the paraventricular nucleus of the hypothalamus (PVH). Mechanistically, we find that cold activates cells within the PVH and pharmacological inactivation of cells blunts cold-induced effects on lipid peroxidation, accumulation of lipid droplets (LDs), and lipolysis in the PVH. Together, these findings suggest that PVH lipid metabolism is cold sensitive and integral to cold-induced broader regulatory responses.

Introduction

Lipid metabolism in peripheral tissues has been extensively studied, including white adipose tissue (WAT) lipolysis (*Grabner et al., 2021*), beiging (*Bartelt and Heeren, 2014*) and brown adipose tissue (BAT) thermogenesis (*Carpentier et al., 2023*); however, an essential but poorly understood element is that of lipids in the central nervous system, particularly in the hypothalamus which plays a crucial role in the regulation of systematic energy metabolism (*Waterson and Horvath, 2015*) and glucose homeostasis (*Pozo and Claret, 2018*). The brain is highly thermal sensitive in that one ºC or less temperature changes can lead to functional alterations of the central nervous system (*Brooks, 1983; Wang et al., 2014*). Lipids provide a major source of energy and heat in the body, however, the mechanism underlying brain lipid metabolism regulations remains a mystery. There is evidence to show that the brain's energy metabolism largely depends on the temperature (*Guyton and Hall, 2006; Yu et al., 2012*). We

67 therefore assume that cold modulates brain lipid metabolism in brain regions that express the
68 genes encoding lipid metabolic enzymes sensitive to ambient temperature. Identifying the brain
69 regions and genes modulated by ambient temperature is of significance in our understandings
70 of the mechanisms of maintaining brain metabolism homeostasis.

71 Here, we combine cold exposure and brain region-selective genetic, molecular, and lipid
72 metabolic assays, coupled with in vivo real-time two-color fiber photometry monitoring of
73 lipid metabolic activity, to define cold-sensitive brain region(s) and lipid metabolism and to
74 elucidate the involved mechanisms.

75

76 ## Results

77

78 **Cold-induced brain region-selective gene expressions of lipid lipolytic markers**

79 To investigate a potential for cold exposure to modulate gene expressions for lipid lipolysis and
80 thermogenesis in the hypothalamus, mice were exposed to a cold (4 °C) chamber for 4 to 6
81 hours, a more physiologically relevant condition. Immediately after the cold challenge, mouse
82 brains were acutely extracted and sectioned in ice-cold oxygenated artificial cerebrospinal
83 fluids (ACSFs). Hypothalamic sections that respectively include the PVH, lateral
84 hypothalamus (LH), dorsomedial hypothalamus (DMH), ventromedial hypothalamus (VMH),
85 and arcuate nucleus (ARC) were transferred to ACSF-containing incubators. Micro-punches of
86 these brain regions were subsequently made for gene assays of lipid metabolic markers.

87 To evaluate the effects of cold on the gene markers of lipolysis, we measured the mRNA
88 levels of two key markers of lipolysis adipose triglyceride lipase (Atgl) and hormone sensitive
89 lipase (Hsl). We observed that cold-challenged male mice showed a significant increase in the
90 gene expressions of the both of Atgl (Fig. $1A_1$) and Hsl (Fig. $1A_2$) selectively in the PVH but
91 not in other brain regions (Fig. 1B-E). We also assayed the gene expressions of thermogenic
92 marker Ucp2 (Uncoupling protein 2) and additional thermogenic factors (Cidea, Prdm16). Cold

did not significantly affect mRNA expressions of these thermogenic markers in all the examined regions in this study (Fig. 1). Cold did not significantly affect gene expressions of these lipolytic and thermogenic markers in female mice (Supplementary Fig. 1). These results suggest that cold exposure (4 ~ 6 h) could induce a rapid lipolytic activity to release fatty acids primarily in the PVH in males. Because cold did not significantly affect lipolytic markers in other regions and did not affect thermogenic markers, we next focused on studying cold-induced lipid mobilization and lipolysis in the PVH in males.

Cold increases the expressions of lipid lipolytic enzymes in the PVH

To verify the cold-induced effects on lipolytic gene expressions, we next stained the protein expressions of ATGL and HSL in PVH sections using antibodies against the ATGL and HSL respectively. Matching with the gene expression results, cold-challenged mice showed significant increases in ATGL (Fig. 2) and HSL (Fig. 3) expressions in both neurons and astrocytes respectively, compared to control mice.

Moreover, we examined whether and how cold modified the phosphorylation of the HSL, a key enzyme in the regulation of lipid lipolysis. After the cold exposure of cohort groups of mice, micro-punches of PVH sections were collected and directly used for western blots of phosphorylated HSL (p-HSL), HSL, and action. Cold significantly increased activation (S660) site phosphorylation of the HSL compared to controls (Fig. 4).

Cold-induced accumulation of lipid droplets (LDs)

It is increasingly appreciated that lipid droplets, endoplasmic reticulum (ER)-derived intracellular neutral lipid storage dynamic organelles (*Olzmann and Carvalho, 2019*), are predominantly accumulated in adipose tissues and liver under normal physiological conditions (*Farese and Walther, 2009; Murphy, 2001*). Also, there is evidence to indicate that glial cells

118 such as astrocytes and tanycytes in the brain accumulate LDs under metabolic and hypoxic
119 stress (*Geller et al., 2019; Smolic et al., 2021*). A recent elegant study shows that hyperactive
120 neurons release fatty acids from phospholipids to formulate LDs in the brain and activation of
121 neurons promotes lipolysis by increasing cytoplasmic lipases (*Ioannou et al, 2019*). These
122 findings suggest that increased neuronal activity and accumulated LDs probably contribute to
123 the cold-induced increase in the lipolytic markers we observed in this study.

124 To probe the mechanism of the upregulation of lipolytic markers in the PVH, we evaluated
125 the ability for cold to accumulate LDs. After the cold challenge, mouse brains were perfused,
126 fixed, and sectioned. Hypothalamic sections containing PVH were stained using the BODIPY
127 493 (BD493), a LD probe which has been well developed and widely applied to measure LD
128 number and area in fixed tissues and live cells respectively (*Geller et al., 2019; Ioannou et al.,*
129 *2019; Liu et al., 2015; Long et al., 2012; Smolic et al., 2020; Spangenburg et al., 2011*).
130 Interestingly, we observed that a short-term (30 min ~ 1 h) cold exposure induced an increase
131 in the LD area in the PVH (Fig. 5A-C). We verified LDs by using the cytoplasmic LD-binding
132 protein perilipin-2 (Fig. 5D-F). To define the cell type selectivity of LD accumulation induced
133 by cold, we co-stained LDs with the BD493, astrocytes with S100b, and neurons with neuronal
134 marker NSE respectively in PVH sections. We observed that cold exposure significantly
135 increased the BD493-positive S100b-expressing astrocytes but not NSE-expressing neurons
136 (Supplementary Fig. 2), consistent with the previous reports that LDs were primarily
137 accumulated in glial cells (*Bailey et al., 2015; Liu et al., 2015; Marschallinger et al., 2020;*
138 *Smolic et al., 2020*). However, a longer (4 ~ 6 h) cold exposure reduced the number of LDs
139 (Supplementary Fig. 3), which might be due to cold-induced liberations of fatty acids from the
140 LDs to mitochondria for β-oxidation.

141

142

143 **Cold increases Fos expressions in PVH**

144 We next examined whether and how cold modified cell activities within the PVH. Mice were
145 placed in a cold chamber before mouse brains were perfused and fixed. PVH sections (40 μm
146 in thickness) were stained using anti-Fos antibodies. Mice subjected to the cold challenge
147 showed increased expressions of the activity indicator Fos in the PVH as compared to control
148 mice (Fig. 6A-C).

149

150 ***In vivo* real-time photometry monitoring of cold-induced lipid peroxidation**

151 As lipid peroxidation is essential in neuronal activity-dependent accumulation of LDs (*Ionanna*
152 *et al., 2019*), we next evaluated the capability for cold to induce lipid peroxidation. Fiber
153 photometry has recently been applied to detect the levels of fluorescent biosensors *in vivo* by
154 us (*Chen et al., 2022*) and others (*Andersen et al., 2023; Sun et al., 2018*). To achieve this goal,
155 we took advantage of the BODIPY581/591 C11 (BD-C11) ratiometric lipid peroxidation sensor,
156 coupled with *in vivo* time-lapse two-color photometry monitoring approach. We developed and
157 validated this approach to simultaneously monitor both red and green signals in one brain
158 region through a single implanted photometry fiber connected to a two-color photometry system,
159 for the BD-C11 sensor as it shifts its fluorescence emission peak from 590 (red) and 510 (green)
160 nm when oxidized. A custom-made Optical fiber multiple Fluid injection Cannula (OmFC)
161 implanted over the PVH was used for both BD-C11 injection and photometry monitoring of
162 the two signals in freely behaving mice. Intra-PVH injection of the BD-C11 sensor through the
163 OmFC was performed 4 h prior to placing the mice in a temperature-controlled chamber. Cold
164 potently increased the BD-C11 ratio (green to red), indicating increased lipid peroxidation (Fig.
165 7A). To verify this result, we treated mice with a lipid soluble antioxidant α-tocopherol (α-TP)
166 to inhibit lipid peroxidation. Compared to vehicle-treated mice (Fig. 7B), prior inhibition of
167 lipid peroxidation with α-TP blunted the cold-induced effects on lipid peroxidation (Fig. 7C).

168 These results demonstrate that cold induces lipid peroxidation in the PVH and that our
169 combined photometry and BD-C11 approach can be reliably applied to evaluate the dynamics
170 of brain lipid metabolism in a spatiotemporal manner.
171
172 **Lipid peroxidation is under the control of cell activity**
173 We next sought to examine whether lipid peroxidation is under the control of cell activity. To
174 examine whether cold alters cell activity, we transduced PVH cells with the Ca^{2+} indicator
175 $GCaMP_{6f}$- and placed the PVH transduced and photometry fiber implanted mice in a cold
176 chamber (Supplementary Fig. 4A). Cold exposure increased the intensity of PVH $GCaMP_{6f}$
177 signals (Supplementary Fig. 4 B and C), consistent with the increased Fos expressions (Fig. 6).
178 To test inhibit cell activity, we utilized the $GABA_A$ receptor agonist muscimol (MUS)
179 (*Barbalho et al., 2009; Sanders and Shekhar, 1995*) and glutamate receptor antagonist
180 Kynurenic acid (KYN) (*Yoshida et al., 2012*). To verify the inhibitory effect of the combined
181 two chemicals, we performed intra-PVH injection of MUS and KYN in PVH $GCaMP_{6f}$ –
182 transduced and fiber implanted mice. Thirty min post the MUS and KYN administration via
183 intra-PVH injection was able to reduce cell activity, as indicated by the decreased intensity of
184 $GCaMP_{6f}$ signals, compared to ventricle treatment (Supplementary Fig. 4D and E).
185 To test whether cell inactivation could diminish the cold-induced effect on lipid
186 peroxidation, intra-PVH injections of MUS and KYN were performed 30 min before placing
187 the previously BD-C11 injected mice in a cold chamber and performing photometry monitoring
188 of BD-C11 signals. Administration of the MUS and KYN prevented the cold-induced increase
189 in the BD-C11 ratio (Fig. 7D), suggesting that cell activation is required for the cold-induced
190 lipid peroxidation.
191
192 **Cell inactivation prevents cold-induced lipolysis**

193 To evaluate lipolysis in the PVH, we performed intra-PVH injections of the EnzCheck lipase
194 substrate through an implanted OmFC. The lipase substrate shifts its fluorescence to emission
195 peak 515 nm (green) in the presence of lipases, and we detected the green signals using our
196 photometry system in a temporal manner. Intra-PVH injection of EnzCheck lipase substrate
197 was performed 4 h before placing mice in a temperature-controlled chamber. Cold induced a
198 potent increase in the green signals generated from the lipase substrate, indicating increased
199 lipolysis (Fig. 8A-B). To verify this, we injected mice with the pan-lipase inhibitor
200 diethylumbelliferyl phosphate (DEUP) via intra-PVT injections to inhibit lipolysis. Cold-
201 induced lipolysis was reduced with the treatment of DEUP compared to vehicle-treated mice
202 (Fig. 8C). These results are consistent with the cold-induced increase in lipolytic markers (Figs.
203 1 - 4), further indicating that cold induces lipolysis in the PVH by increasing cytoplastic lipases.
204 To examine whether cell activity is required for the cold-induced lipolysis, in cohort groups of
205 PVH-implanted mice which were treated with the lipase substrate via intra-PVH injections, we
206 performed intra-PVH injections of the MUS and KYN 30 min before placing the mice in a cold
207 chamber. Administration of MUS and KYN prevented the cold-induced conversion of the
208 lipase substrate, indicating decreased lipolytic activity (Fig. 8D). These findings suggest that
209 cold induces a rapid activity-dependent lipid lipolytic effect.
210

211 **Cell inactivation reduces cold-induced LD accumulation**

212 To verify our results of LDs detected in the fixed tissues (Fig. 5), we next performed time-lapse
213 photometry monitoring of dynamics of LDs *in vivo* in freely behaving mice. To achieve this
214 goal, we implanted an OmFC cannula in PVH for LD marker BD493 (green) injections and
215 monitoring in mice. Matching with the results collected from the fixed sections, cold induced
216 an increase in the intensity of BD493 signals (Fig. 9A and B). This result indicates that cold
217 increases the accumulation of LDs which could be directly used for lipolysis by releasing fatty

218 acids to mitochondria for β-oxidation. The lipid soluble antioxidant α-TP blocked the cold-
219 induced LD accumulation (Fig. 9 C). To define a role of cell activity in modulating LDs, we
220 performed intra-cannula injections of both MUS and KYN in BD493-injected mice in the PVH.
221 MUS and KYN administration blunted the cold-induced accumulation of LDs, as cold failed
222 to increase the BD493 signals in MUS and KYN treated mice compared to controls (Fig. 9D).
223

224 **Discussion**

225 For survival, it is crucial for individuals to precisely modulate lipid metabolism in both the
226 peripheral tissues and brain in mammalian animals. Extensively studies have been focused on
227 lipid metabolism in peripheral tissues particularly adipose tissues, while little or nothing was
228 known about that in the brain. This was probably in part because of limited techniques. By
229 taking advantage of combined coordinated neurobiology methods and lipid metabolic assays,
230 we provided in this study the *in vivo* evidence that cold is capable to induce acute cell activity-
231 dependent central nervous system lipid metabolic activities, including lipid peroxidation and
232 mobilization, lipid droplet formation, and lipid lipolysis in the hypothalamus. These results fill
233 in a missing but important gap in our understanding of brain region selective lipid metabolism
234 in physiological conditions such as cold applied in this study. Also, our *in vivo* time-lapse fiber
235 photometry approach detecting probe-labelled lipid metabolites would provide an alternative
236 method to evaluate the dynamics of lipid metabolism in live animals. We believe our studies
237 will also be paradigmatic for understanding abnormal lipid metabolism in brain regions
238 modifying energy metabolism in metabolic disorders such as obesity.

239 The third ventricle adjacent PVH is a conserved brain region (*Machluf et al., 2011*),
240 composed of different cell populations including those multiple brain regions-projecting
241 parvocellular neurons and magnocellular neurons. Particularly, PVH plays varied crucial roles
242 in modulating the hypothalamic-pituitary-adrenal (HPA) axis and the hypothalamic-pituitary-

243 thyroid axis (HPT) (*Swanson et al., 1983*). This determines a key role of the PVH in modulating
244 body functions, energy metabolism and glucose homeostasis in health and disease. Our
245 findings in this study show that cold increases the expressions levels of Fos, lipid peroxidation,
246 LD accumulation, and lipolytic markers in the PVH. These findings reveal a new role for the
247 PVH in preventing fatty acid toxicity in pathological conditions.

248 Activated neurons would induce phospholipid peroxidation to release toxic fatty acids.
249 One recent elegant study (*Ioannou et al., 2019*) shows that nearby astrocytes have the capacity
250 to endocytose neuron-released fatty acids (FAs), store them in LDs, and liberate FAs from LDs
251 through lipolytic processes to mitochondria for β-oxidation. Consistently, our data in this study
252 demonstrate that cold-induced lipid peroxidation and lipolysis in the brain are also under the
253 control of cell activities. Our data also show that cold induces increased expressions of ATGL
254 and HSL in both neurons and astrocytes (Figs. 2 and 3). These findings suggest that both
255 neurons and astrocytes play important roles in inducing lipid metabolism and fatty acid
256 accumulations in the brain in certain physiological and pathological conditions.

257 Lastly, the brain is highly thermal sensitive (*Brooks, 1983*). Identifying brain regions
258 sensitive to ambient temperature is significant and important in our understandings of brain
259 energy metabolism and homeostasis, as which might provide potential targetable sites in the
260 treatment of brain lipid metabolism-associated neurological disorders.

261

262 **Methods**

263 Experimental protocols were approved by the Institutional Animal Care and Use Committees
264 at the Albert Einstein College and conducted following the U.S. National Institutes of Health
265 guidelines for animal research.

266

267 **Animals**

268 C57/BL6J wild type mice (#000664, Jackson Laboratory) have been described previously and

are available from The Jackson Laboratory. Both male and female mice (age 8-12 weeks) were used at the start of experiments. Mice were group-housed 3–5 mice per cage in humidity- and temperature (22–25 °C)-controlled rooms on a 12-hour light:dark cycle (lights on from 8:00 a.m. to 8:00 p.m.) with *ad libitum* access to water and mouse regular chow (#5001, LabDiet). Mice were single-caged after they received viral transductions with or without guide or optic fiber cannula insertion until all the experimental procedures were finished.

Pharmacology

All the chemicals were purchased from Sigma except where noted. For the experiments requiring intra-PVH injections, an injector with 1-mm extension beyond the custom-made optical fiber multiple fluid injection cannula (OmFC) (Doric Lens) implanted over the PVH was attached by polyethylene tubing to a Hamilton syringe. The injection was performed at a speed of 50 nl per min for 4 min using a matched fluid injector consisiting of a 1.25 mm ferrule and a sleeve connector, and the injector was withdrawn 10 min after the final injection. Grip cement (DENTSPLY) was used to anchor the cannula to the skull, and a plug was inserted to keep the cannula from becoming clogged when the injector was not in place. Mice were then returned to the home cage for one week at least before the experiments. The amount for intra-PVH injection was 200 nl of vehicle or chemicals (in μM): 100 BODIPY™ 493/503 (D3922, Invitrogen), 100 BODIPY™ 581/591 C11 (D3861, Invitrogen), 1 MitoSOX™ Mitochondrial Superoxide Indicators (M36005, Invitrogen), 1 EnzChek™ Lipase Substrate 505/515 (E33955, Invitrogen), 100 Diethylumbelliferyl phosphate (D7692, Sigma), and 500 α-Tocopherol (#258024, Sigma); or 200 nl of 250 pmol Muscimol (M1523, Sigma) and 100 mol Kynurenic acid (K3375, Sigma).

Stereotaxic OmFC implantations for intra-PVH injections and photometry.

Following our previously documented protocols (*Chen et al, 2022; Zhang et al., 2020*), mice were anesthetized with 3% isoflurane to induce the anesthesia and with 1.5–2.0% isoflurane to maintain anesthesia during the surgery and placed in a stereotaxic frame (Kopf Instruments). A small incision was made in the skin of the head, a small hole was drilled on the skull, and mice were implanted with a custome-made optical fiber multiple fluid injection cannula (OmFC) (Doric Lens) over the PVH (coordinates from bregma: AP -0.8 mm, 0.2 mm from midline, DV -4.0 mm). The cannula was fixed to the skull with stainless steel screws and dental cement. After the surgery, all mice received meloxicam (5 mg/kg) and continued to be housed

302 individually. Two weeks after surgery, the mice were briefly anesthetized and inserted with the
303 fluid injector (with 1 mm protrusion) into PVH. For intra-PVH injection, the injector was
304 attached to a Hamilton syringe through a polyethylene tube and the mice received 200 nl of
305 vehicle, chemicals as listed in the Pharmacology section, or viral vectors (AAV_5-CamKII-
306 $GCaMP_{6f}$-WPRE-SV40, addgene#100834, titer, 2.3×10^{13} GC/ml) or chemicals as stated
307 above, at a rate of 50 nl/min.
308
309 **Micro-punches of hypothalamic nuclei**
310 As described in our previously published studies (*Qi and Yang, 2015; Chen et al, 2022; Zhang*
311 *et al., 2020*), acute brain slices that include hypothalamic PVH, LH, DMH, VMH, and ARC
312 respectively were prepared. Briefly, mice were first placed in a cold chamber (4 °C) for 30 min
313 or 4-6 h respectively, as described in the text and figure legends. After the cold exposure, mice
314 were deeply anesthetized with isoflurane and decapitated. The mouse brains were dissected
315 rapidly and placed in ice-cold oxygenated (95% O_2 and 5% CO_2) solution containing the
316 following (in mM): 110 choline chloride, 26.2 D-glucose, 2.5 KCl, 1.25 NaH_2PO_4, 2 $CaCl_2$, 7
317 $MgSO_4$, 11.6 Na-L-ascorbic acid, and 3.1 Na-pyruvate. Coronal brain slices (280 μm thick)
318 were cut with a vibratome (Leica; VT 1200 S) and maintained in an incubation chamber
319 containing artificial cerebrospinal fluids (aCSFs) (in mM): 119 NaCl, 25 $NaHCO_3$, 11 D-
320 glucose, 2.5 KCl, 2.5 $CaCl_2$, 1.3 $MgSO_4$, and 1 NaH_2PO_4. Micro-punches of the PVH, LH,
321 DMH, VMH and ARC were performed using a punch (1.5 mm diameter; Stoelting#57403) or
322 a pipette tip (1.5 mm diameter). Six micro-punches of each region were obtained from each
323 mouse were respectively collected and immediately placed in 200 μl Trizol reagent (Invitrogen)
324 and stored at -80 °C until analysis.
325
326 **Total RNA extractions and Real-time qPCR (RT-qPCR)**
327 Total RNA was extracted using Trizol reagent (Invitrogen) according to manufacturer's
328 instruction. Briefly, the collected tissues were lysed in 200 μl of Trizol reagent (Invitrogen) and
329 40 μl of chloroform was added into each tube and subsequently vortexed for 15 s. After
330 incubation for 2 min, centrifuged at 12,000 x g for 10 min (4 °C). The aqueous phase was
331 transferred to fresh tube and equal volume of isopropanol was added. The tube was incubated
332 for 20 min and centrifuged at 12,000 × g for 10 min (4 °C). The RNA pellet was washed with
333 70% ethanol by vortex and centrifuged at 12,000 x g for 10 min (4 °C). cDNA was synthesized
334 by High-Capacity cDNA Reverse Transcription Kit (Applied Biosystems) following the

335 manufacturer's instructions. Real-time qPCR was performed using QuantStudio 3 instruments
336 (Applied Biosystems). The mixture for qPCR reaction was prepared in a final volume of 20 µl
337 containing 1 µl cDNAs and 10 µl of LightCycler 480 SYBR Green I Master (Roche) in the
338 presence of primers at 500 nM. The specific primer sequences used were the following:
339 The specific primer sequences used were the following:
340 ATGL forward, 5′-CCAACACCAGCATCCAGT-3′;
341 ATGL reverse, 5′-CAGCGGCAGAGTATAGGG-3′;
342 HSL forward, 5′-CGCCATAGACCCAGAGTT-3′
343 HSL reverse, 5′-TCCCGTAGGTCATAGGAGAT-3′;
344 Cidea forward, 5′-TGCTCTTCTGTATCGCCCAGT-3′
345 Cidea reverse, 5′-GCCGTGTTAAGGAATCTGCTG-3′;
346 Prdm16 forward, 5′-CCACCAGCGAGGACTTCAC-3′
347 Prdm16 reverse, 5′-GGAGGACTCTCGTAGCTCGAA-3′;
348 Ucp2 forward, 5′-CAGAGCACTGTCGAAGCCTA-3′
349 Ucp2 reverse, 5′-GTATCTTTGATGAGGTCATA-3′;
350 Actb forward, 5′-GCTGTCCCTGTATGCCTCT-3′
351 Actb reverse, 5′-GTCTTTACGGATGTCAACG-3′;.
352 The relative level of expression was calculated using the comparative $2^{-\Delta\Delta CT}$ method.
353
354 **Two-color two-channel fiber photometry (FP)**
355 Briefly, three excitation wavelengths were used: 560, 505 / 490, and 405 nm. Excitation lights
356 were generated through fiber-coupled two connectorized LEDs (CLED_560 for 560 nm;
357 CLED_505 / 490 for 505 or 490 nm; CLE_405 for 405 nm; Doric Lenses) driven by a four-
358 channel LED driver (LEDD_4; Doric Lenses). The LEDD_4 was controlled by a fiber
359 photometry console (FPC; Doric Lenses) connected to a computer. Excitation lights were
360 passed through two fluorescence MiniCubes (iFMC6_IE(400-410)_E1(460-490)_F1(500-
361 540)_E2(555-570)_F2(580-680)_S)-6 ports with 2 integrated photodetector heads. The single
362 detector measures both signals within the fluorescence detection windows from 500-540 nm
363 and 580-680 nm band. The combined excitation light was sent into a patch cord made of a 400
364 µm core, 0.48 NA, low-fluorescence optical fiber (Doric Lenses). The patch cord was
365 connected to the implanted OmFC consisting of a 1.25 mm diameter optic fiber via a sleeve
366 (Doric Lenses; Zirconia Sleeve 1.25 mm with black cover; Sleeve_ZR_1.25-BK). Both green

367 and red fluorescence signals were collected through the same patch cord and passed through
368 the same Minicube and focused onto a Fluorescence Detector Head (FDH; Doric Lenses). The
369 photometry experiments were run in a Lock-in mode, and the acquisition rate was set to 12.0
370 ksps*C controlled by Doric Neuroscience Studio software (Doric Lenses). The FP experiments
371 were performed 5 min after connecting the optic fibers to the animals. We processed the signals
372 using the Doric Neuroscience Studio software (V5.3.3.14) to calculate the normalized
373 fluorescence variation of the images (ΔF/F), and averaged the signals at 1-s bins. To avoid or
374 minimize bleaching over time, we performed patch cord photobleaching for 12 h before each
375 experiment, reduced the illumination power outputs as much as possible, and recorded the
376 signals for 30 s every 5 min. We used a rotary joint for long-term photometry recordings in
377 freely moving animals.
378
379 **Brain histology and immunofluorescence**
380 Mice were euthanized and transcardially perfused with 1 x phosphate buffered saline (PBS, pH
381 7.4) followed by 4% paraformaldehyde in phosphate buffer (PFA, pH 7.2). Mouse brains were
382 removed and post-fixed in 4% PFA overnight. Fixed brains were transferred to 30% sucrose in
383 PBS for cryoprotection. Next, 30 μm coronal sections were cut in a freezing cryostat (Leica).
384 For immunofluorescence, slices were washed three times in 1 x PBS for 10 min each and heat-
385 incubated with target antigen retrieval solution (Invitrogen) for 2 min at 95 °C. And then, the
386 slices were washed three times in 1 x PBS for 10 min each, followed by permeabilization in 1%
387 triton X-100 solution in 1 x PBS for 40 min at room temperature. After blocking for 1 hour at
388 room temperature, the slices were incubated with a mouse Fos antibody (1:150, sc-166940
389 AF647, Santa Cruz Biotechnologies), rabbit ATGL (1:150, bs-3831R-BF488, Bioss), rabbit
390 HSL (1:150, bs-3223R-BF488, Bioss), rabbit NSE (1:200, bs-10445R-BF594, Bioss), and
391 mouse S100b (1:200, bsm-10832-BF594, Bioss), respectively, for overnight at 4 °C in the dark.
392 The slices were then rinsed three times in 0.1% triton X-100 solution in 1 x PBS for 10 min
393 each. For lipid droplet staining, slices were washed three times in 1 x PBS for 10 min each and
394 then incubated with 1% triton X-100 solution in 1 x PBS for 40 min. After blocking for 1 hour,
395 the slices were stained with 20 μg/mL BODIPY 493/503 (Invitrogen, D3922) for 4 hours at
396 room temperature in the dark. After the incubation, the slices were rinsed three times in 0.1%
397 triton X-100 solution in 1 x PBS for 10 min each. For BODIPY 493/503 co-staining with
398 perilipin-2, NSE, and S100b respectively, after permeabilization in 1% triton X-100 solution
399 in 1 x PBS for 40 min and blocking for 1 hour at room temperature, the slices were incubated

with rabbit perilipin-2 (1:200, CL594-15294, Proteintech), rabbit NSE, and mouse S100b antibodies, respectively, for overnight at 4 °C in the dark. The slices were then washed three times in 0.1% triton X-100 solution in 1x PBS for 10 min and incubated with 20 μg/mL BODIPY 493/503 (Invitrogen, D3922) for 4 hours at room temperature in the dark and then washed three times in 0.1% triton X-100 solution in 1x PBS for 10 min each time. The stained slices were dried and mounted with mounting medium (0100–20, Southern Biotech). Images were taken using the All-in-One Fluorescence Microscope (BZ-X800E Keyence) and analyzed using the BZ-X800 Analyzer (Keyence).

PVH tissue western blot

Acute coronal brain slices (260-μm thickness) were collected following the procedures as stated in the above. Six micro-punches of PVH sections from each mouse were made and immediately placed in 40 μl cold lysis buffer containing 50 mM Tris-HCl, 150 mM NaCl, 0.25% Na-deoxycholate, 1 mM EDTA, 1% NP-40, 1 mM PMSF (20 mM PMSF in 100% ethanol), and 1 protease inhibitor tablet (A32955, Thermo Scientific). The samples were homogenized in lysis buffer and centrifuged at 14,000 × rpm at 4 °C for 20 min. The supernatants were transferred to a fresh tube and used for Bradford assay to quantify the protein concentration. Equal amounts of protein from each sample were denatured and boiled at 100 °C for 5 min. Proteins were separated by electrophoresis in 10% SDS-PAGE gel and transferred to PVDF membrane. The membrane was blocked with Protein-Free blocking buffer (927-80001, LI-COR) for 1 h and incubated overnight with relevant primary antibodies at 4 °C, including the p-HSL (1:1,000, PA5-64494, Invitrogen), HSL (1:1,000, PA5-17196, Invitrogen), and β-actin (1:5,000, MAB8929, R&D Systems). After washing in TBST, the membranes were incubated with secondary antibodies for 1 hour and a subsequent TBST washing. Images were acquired using Odyssey Classic Imager (LI-COR). The band intensity of HSL and p-HSL was quantified using the ImageJ.

Author contributions: H.Y.M. and Y.Y. conceived, designed, and performed the experiments, analyzed data, and wrote the manuscript. Y.Y.Y. edited the manuscript.

Acknowledgements: We thank all the members of the Yang laboratory for discussion and critical comments on this study. We thank the Doric Lenses for helping us build and adjust the two-channel two-color photometry rig. For the genetically encoded calcium indicator $GCaMP_{6f}$

plasmids, we thank Dr. James M Wilson for depositing the plasmid of pENN-AAV-CamKII-GCaMP$_{6f}$-WPRE-SV40. This work was supported by the NIH (R01 DK112759, R01 DK135717 to Y.Y.) and Einstein Research Foundation.

Competing interests: Authors declare no competing interests.

Data and materials availability: All data are available in the main text or the supplementary materials.

References

Andersen M, Tsopanidou A, Radovanovic T, Compere VN, Hauglund N, Nedergarrd M et al. (2023) Using fiber photometry in mice to estimate fluorescent biosensor levels during sleep. *Bio Protoc* **13**:e4734.

Bailey AP, Koster G, Guillermier C, Hirst EM, MacRae JI, Lechene CP et al. (2015) Antioxidant role for lipid droplets in a stem cell niche of drosophila. *Cell* **163**:340-353.

Barbalho CA, Nunes-de-Souza R, Canto-de-Souza A (2009) Similar anxiolytic-like effects following intra-amygdala infusions of benzodiazepine receptor agonist and antagonist: evidence for the release of an endogenous benzodiazepine inverse agonist in mice exposed to elevated plus-maze test. *Brain Res* **1267**:65-76.

Bartelt A, Heeren J (2014) Adipose tissue browning and metabolic health. *Nature Reviews Endocrinology* **10**:24-36.

Brooks VB (1983) Study of brain function by local, reversible cooling reviews of physiology, biochemistry and pharmacology. Vol 95 Berlin; Heidelberg: Spring, 1-109.

Chen D, Qi Y, Zhang J, Yang Y (2022) Deconstruction of a hypothalamic astrocyte-white adipocyte sympathetic axis that regulates lipolysis in mice. *Nat Commun* **13**:7536.

Carpentier AC, Blondin DP, Haman F, Richard D (2023) Brown adipose tissue-a translational perspective. *Endocrine Reviews* **44**:143-192.

Farese RV Jr, Walther TC (2009) Lipid droplets finally get a little R-E-S-P-E-C-T. *Cell* **139**:855-860.

Geller S, Arribat Y, Netzahualcoyotzi C, Lagarrigue S, Carneiro L, Zhang L et al. (2019) Tanycytes regulate lipid homeostasis by sensing free fatty acids and signaling to key hypothalamic neuronal populations via FGF21 secretion. *Cell Metab.* **30**:833-844.

Grabner GF, Xie H, Schweiger M, Zechner R (2021) Lipolysis: cellular mechanisms for lipid mobilization from fat stores. *Nat Metab.* **3**:1445-1465.

Guyton AC, Hall JE (2006) Textbook of medical physiology. Philadelphia:Elsevier Saunders.
Delgado JM, Hanai T. 1996. Intracerebral temperatures in free-moving cats. *Am J Physiol*. **211**:755-769.

Ioannou MS, Jackson J, Shen SH, Chang CL, Weigel AV, Liu H et al. (2019) Neuron-astrocyte metabolic coupling protects against activity-induced fatty acid toxicity. *Cell* **177**:1522-1535.

Kajimura S, Saito M (2014) A new era in brown adipose tissue biology: molecular control of brown fat development and energy homeostasis. *Annu Rev Physiol*. **76**:225-249.

Liu L, Zhang K, Sandoval H, Yamamoto S, Jaiswal M, Sanz E et al. (2015) Glial lipid droplets and ROS induced by mitochondrial defects promote neurodegeneration. *Cell* **160**:177-190.

Long AP, Manneschmidt AK, VerBrugge B., Dortch MR, Minkin SC, Prater KE et al. (2012) Lipid droplet De Novo formation and fission are linked to the cell cycle in fission Yeast. *Traffic* **13**:705-714.

Machluf Y, Gutnick A, Levkowitz G (2011) Development of the zebrafish hypothalamus. *Ann NY Acad Sci*. **1220**:93-105.

Mcelligott JG, Melzack R (1967) Localized thermal changes evoked in the brain by visual and auditory stimulation. *Exp Neurol* **17**:293-312.

Marschallinger J, Iram T, Zardeneta M, Lee SE, Lehallier B, Haney MS et al (2020) Lipid-droplet-accumulating microglia represent a dysfunctional and proinflammatory state in the aging brain. *Nat Neurosci* **23**:194-208.

Moser EI, Mathiesen LI (1996) Relationship between neuronal activity and brain temperature in rats. *Neuroreport* **7**:1876-1880.

Murphy DJ (2001) The biogenesis and functions of lipid bodies in animals, plants and microorganisms. *Prog. Lipid Res*. **40**:325-438.

Olzmann JA, Carvalho P (2019) Dynamics and functions of lipid droplets. *Nat Rev, Mol Cell Biol* **20**:137-155.

Pozo M, Claret M (2018) Hypothalamic control of systemic glucose homeostasis: the pancreas connection. *Trends Endocrinol Metab.* **29**:581-594.

Qi Y, Yang Y. 2015. Hunger states control the directions of synaptic plasticity via switching cell type-specific subunits of NMDA receptors. *J Neurosci*. **35**:13171-13182.

Sanders SK, Shekhar A (1995) Regulation of anxiety by GABAA receptors in the rat amygdala. *Pharmacol Biochem Behav*. **52**:701-706.

Smolic T, Tavcar P, Horvat A, Cerne U, Vasle AH, Tratnjek L *et al.* (2020) Astrocytes in stress accumulate lipid droplets. *Glia* **69**:1540-1562.

Spangenburg EE, Pratt SJP, Wohlers LM, Lovering RM (2011) Use of BODIPY (491/503) to

visualize intramuscular lipid droplets in skeletal muscle. Methodology Report. Volume 2011.

Sun F, Zeng J, Jing M, Zhou J, Feng J, Owen SF *et al.* (2018) A genetically encoded fluorescent sensor enables rapid and specific detection of dopamine in flies, fish, and mice. *Cell* **174**:4810496.

Swanson LW, Sawchenko PE (1983) Hypothalamic integration: organization of the paraventricular and supraoptic nuclei. *Annu Rev Neurosci*. **6**:269-324.

Thornton K (2003) The electrophysiological effects of a brain injury on auditory memory functioning. The QEEG correlates of impaired memory. *Arch Clin Neuropsychol*. **18**:363-378.

Waterson MJ, Horvath TL (2015) Neuronal regulation of energy homeostasis: beyond the hypothalamus and feeding. *Cell Metab.* **6**:962-970.

Yoshida J, Tomonaga S, Ogino Y, Nagasawa M, Kurata K, Furuse M (2012) Intracerebroventricular injection of kynurenic acid attenuates corticotrophin-releasing hormone augmented stress responses in neonatal chicks. *Neurosci*ence **220**:142-148.

Yu Y, Hill AP, Mccormick DA (2012) Warm body temperature facilitates energy efficient cortical action potentials. *PLoS Comput Biol*. **8**:e1002456.

Zhang J, Chen D, Sweeney P, Yang Y (2020) An excitatory ventromedial hypothalamus to paraventricular thalamus circuit that suppresses food intake. *Nat Commun*. **11**:6326.

Figure Legends

Figure 1. Brain region selective responses to cold.

Micro-punches of PVH, LH, DMH, VMH, and ARC were made from male mice exposed to a cold chamber for 4-6 h, which were directly used for RT-qPCR of the gene markers of lipolysis and thermogenesis. (A_1-A_5) Group data of the lipolytic marker *ATGL* (A_1) and *HSL* (A_2) as well as thermogenic marker *Ucp2* (A_3), *Cidea* (A_4) and *Prdm16* (A_5) in the PVH. (B_1-B_5) Group data of the lipolytic marker *ATGL* (B_1) and *HSL* (B_2) as well as thermogenic marker *Ucp2* (B_3), *Cidea* (B_4) and *Prdm16* (B_5) in the LH.

(C_1-C_5) Group data of the lipolytic marker *ATGL* (C_1) and *HSL* (C_2) as well as thermogenic marker *Ucp2* (C_3), *Cidea* (C_4) and *Prdm16* (C_5) in the DMH. (D_1-D_5) Group data of the lipolytic marker *ATGL* (D_1) and *HSL* (D_2) as well as thermogenic marker *Ucp2* (D_3), *Cidea* (D_4) and *Prdm16* (D_5) in the VMH. (E_1-E_5) Group data of the lipolytic marker *ATGL* (E_1) and *HSL* (E_2) as well as thermogenic marker *Ucp2* (E_3), *Cidea* (E_4) and *Prdm16* (E_5) in the ARC. Data represent mean ± s.e.m. Student *t* tests were performed. $*p<0.05$. Each dot represents one animal in each group of all the panels.

566 **Figure 2. Cold increases protein expressions of ATGL in neurons and astrocytes in PVH.**
567 Control or cold (4- 6)-challenged mice were perfused and fixed. Mouse brains were sectioned.
568 ATGL, NSE, and S100b were stained using relevant antibodies respectively. (A)
569 Representative images of ATGL (green), NSE (red), and ATGL/NSE overlay (yellow) signals
570 in PVH sections from cold-challenged mouse. (B) Group data of relative ATGL/NSE overlay
571 signals to total NSE signals in control and cold-challenged mice (n=5 each group). (C) Group
572 data of relative ATGL/S100b overlay signals to total S100b signals in control and cold-
573 challenged mice (n=5 each group). Data represent mean ± s.e.m. Student *t* tests were performed.
574 ***p<0.001, *p<0.05. Scale bar, 100 μm for (A). PVH, paraventricular of hypothalamus; 3rd
575 V, third ventricle.
576
577 **Figure 3. Cold increases HSL protein expressions in both neurons and astrocytes in PVH.**
578 Control or cold (4- 6)-challenged mouse brains were sectioned. HSL, NSE, and S100b were
579 respectively co-stained using relevant antibodies. (A) Representative images of HSL (green),
580 NSE (red) and HSL/NSE overlay (yellow) signals in PVH sections from cold-challenged
581 mouse. (B) Group data of relative HSL/NSE overlay signals to total NSE signals in control and
582 cold-challenged mice (n=5 each group). (C) Group data of relative HSL/S100b overlay signals
583 to total S100b signals in control and cold-challenged mice (n=5 each group). Data represent
584 mean ± s.e.m. Student *t* tests were performed. ***$p < 0.001$, *$p < 0.05$. Scale bar, 100 μm for
585 (A). PVH, paraventricular of hypothalamus; 3rd V, third ventricle.
586
587 **Figure 4. Cold increases the level of phosphorylated HSL in PVH.**
588 Micro-punches of PVH were collected in control and cold (4- 6)-challenged mice, which were
589 used for (A) western blots of p-HSL (Ser660), HSL, and β-action. (B) Group data of p-HSL
590 fold change to HSL (n = 6 each group). Data represent mean ± s.e.m. Student *t* tests were
591 performed. ** $p < 0.01$. Each dot represents one mouse.
592
593 **Figure 5. Cold-induced LD accumulation.**
594 Control or cold (30 min~1 h)-challenged mice were perfused and fixed. Mouse brains were
595 sectioned. LDs in the PVH were labelled using BODIPY493 (BD493). (A, B) Representative
596 images of BD493 signals in PVH sections from one control (A) and one cold-challenged mouse
597 (B). (C) Group data of relative BD493-labelled area in PVH in control and cold-challenged
598 mice (n = 6 each group). (D-F) Sample images of BD493 (D) and perilipin2 (PLIN2) (E) and

599 overlay (F) signals in the PVH. Data represent mean ± s.e.m. Student *t* tests were performed.
600 ****$p < 0.0001$. Scale bars, 50 μm for (A, B), and 1 μm for (D-F). PVH, paraventricular of
601 hypothalamus; 3rd V, third ventricle.
602
603 **Figure 6. Cold increased Fos expressions in the PVH**.
604 Control or cold-challenged mouse brains were perfused and fixed and sectioned. Fos in the
605 PVH were labelled using anti-Fos antibodies. (A) Representative images of Fos signals in PVH
606 from one control (top) and one cold-challenged mouse (bottom). (B) Group data of Fos-positive
607 cells in PVH in control and cold-challenged mice (n = 5 each group). Data represent mean ±
608 s.e.m. Student *t* tests were performed. **$p<0.01$. Scale bars, 100 μm for (A). 3rd V, third
609 ventricle.
610
611 **Figure 7. Cold-induced cell activity-dependent lipid peroxidation in the PVH**.
612 Mice were injected with the lipid peroxidation indicator BD-C11 in the PVH via the implanted
613 OmFC cannula 4 h before placing them in a temperature-controlled chamber. Two-color fiber
614 photometry was applied for time-lapse monitoring of BD-C11 convertion via the optic fiber of
615 the OmFC. (A) Representative traces of real-time photometry monitoring of red and green
616 signals simultaneously. (B-D) Group data of relative BD-C11 ratio to baseline in mice treated
617 with vehicle (B, n=6), α-TP (C, n= 4), and KYN+MUS (D, n=4). Data represent mean ± s.e.m.
618 Student *t* tests were performed.
619
620 **Figure 8. Cold-induced cell activity-dependent lipid lipolysis**.
621 Mice were injected with the lipase substrate in the PVH via the implanted OmFC cannula 4 h
622 before placing them in a temperature-controlled chamber. Two-color fiber photometry was used
623 for time-lapse monitoring of lipase substrate convertion via the optic fiber of the OmFC. (A)
624 Representative traces of real-time photometry monitoring of green signals. (B-D) Group data
625 of lipase substrate convertion in mice treated with vehicle (B, n=4), α-TP (C, n=4), and
626 KYN+MUS (D, n=4). Data represent mean ± s.e.m. Student *t* tests were performed.
627
628 **Figure 9. Cold-induced cell activity-dependent LD accumulation.**
629 Mice were injected with the LD marker BODIPY493 in the PVH via the OmFC cannula 4 h
630 before placing them in a temperature-controlled chamber. Fiber photometry was used for time-

631 lapse monitoring of BODIPY493 signals via the optic fiber of the OmFC. (A) Representative
632 traces of real-time photometry monitoring of BODIPY493 signals. (B-D) Group data of
633 BODIPY493 in mice treated with vehicle (B, n=4), α-TP (C, n= 4), and KYN+MUS (D, n=6).
634 Data represent mean ± s.e.m. Student *t* tests were performed.
635
636
637
638
639
640
641
642
643

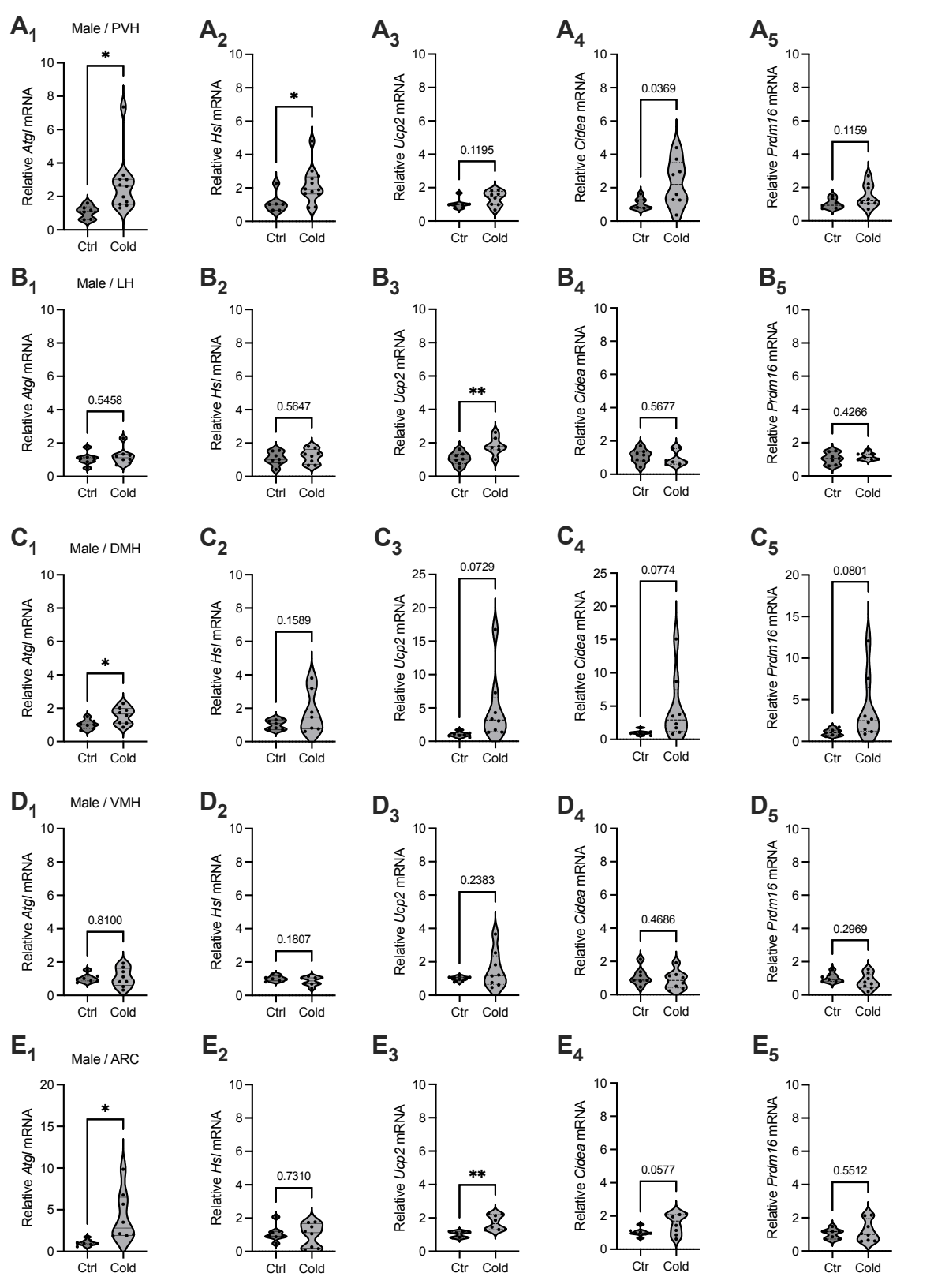
A1
Male / PVH
Relative Atgl mRNA
*
Ctrl
Cold
A2
Relative Hsl mRNA
*
Ctrl
Cold
A3
Relative Ucp2 mRNA
0.1195
Ctr
Cold
A4
Relative Cidea mRNA
0.0369
Ctr
Cold
A5
Relative Prdm16 mRNA
0.1159
Ctr
Cold
B1
Male / LH
Relative Atgl mRNA
0.5458
Ctrl
Cold
B2
Relative Hsl mRNA
0.5647
Ctrl
Cold
B3
Relative Ucp2 mRNA
**
Ctr
Cold
B4
Relative Cidea mRNA
0.5677
Ctr
Cold
B5
Relative Prdm16 mRNA
0.4266
Ctr
Cold
C1
Male / DMH
Relative Atgl mRNA
*
Ctrl
Cold
C2
Relative Hsl mRNA
0.1589
Ctrl
Cold
C3
Relative Ucp2 mRNA
0.0729
Ctr
Cold
C4
Relative Cidea mRNA
0.0774
Ctr
Cold
C5
Relative Prdm16 mRNA
0.0801
Ctr
Cold
D1
Male / VMH
Relative Atgl mRNA
0.8100
Ctrl
Cold
D2
Relative Hsl mRNA
0.1807
Ctrl
Cold
D3
Relative Ucp2 mRNA
0.2383
Ctr
Cold
D4
Relative Cidea mRNA
0.4686
Ctr
Cold
D5
Relative Prdm16 mRNA
0.2969
Ctr
Cold
E1
Male / ARC
Relative Atgl mRNA
*
Ctrl
Cold
E2
Relative Hsl mRNA
0.7310
Ctrl
Cold
E3
Relative Ucp2 mRNA
**
Ctr
Cold
E4
Relative Cidea mRNA
0.0577
Ctr
Cold
E5
Relative Prdm16 mRNA
0.5512
Ctr
Cold

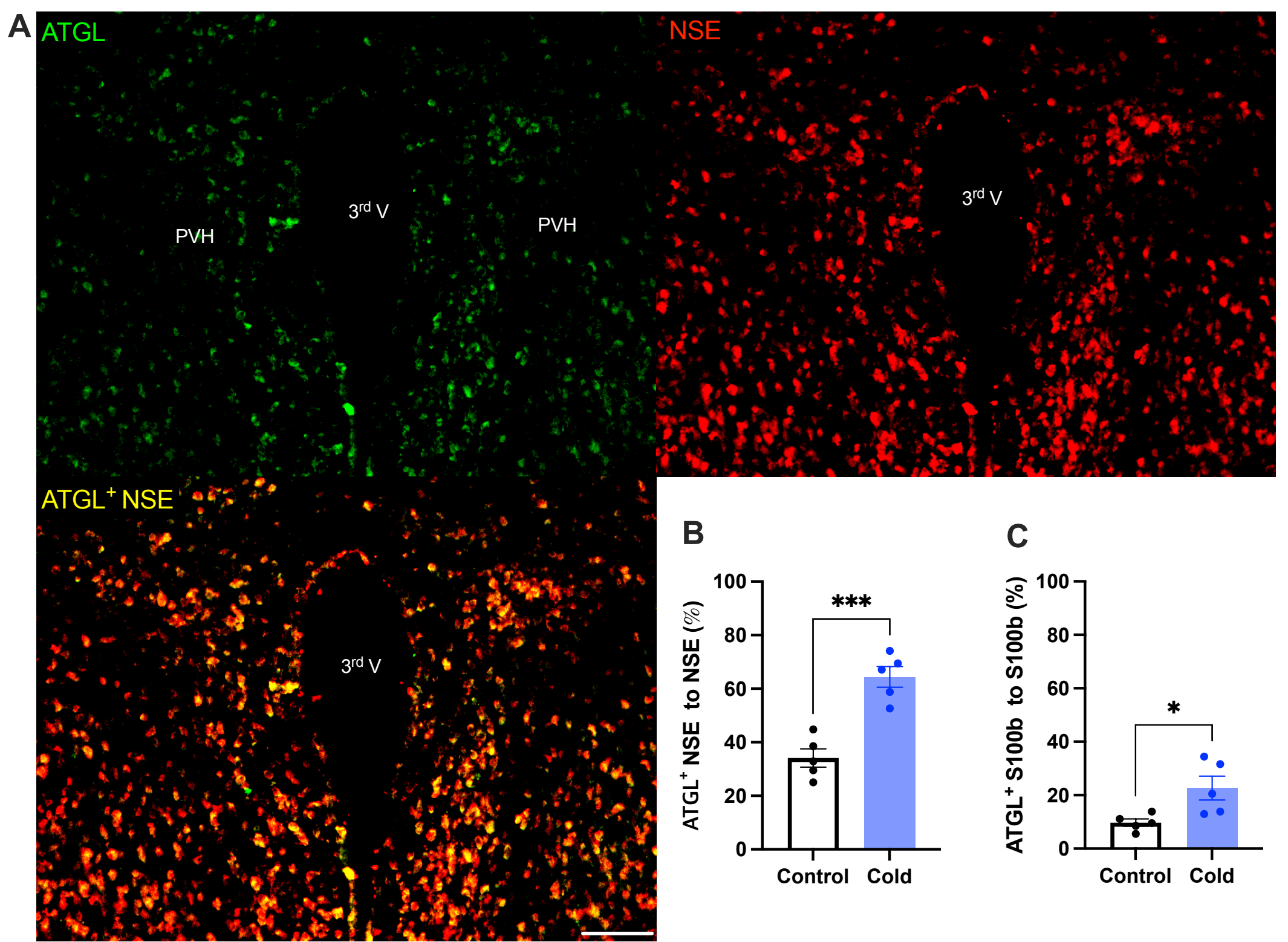
A
ATGL
PVH
3rd V
PVH
NSE
3rd V
ATGL+ NSE
3rd V
B
ATGL+ NSE to NSE (%)
100
80
60
40
20
0
***
Control
Cold
C
ATGL+ S100b to S100b (%)
100
80
60
40
20
0
*
Control
Cold

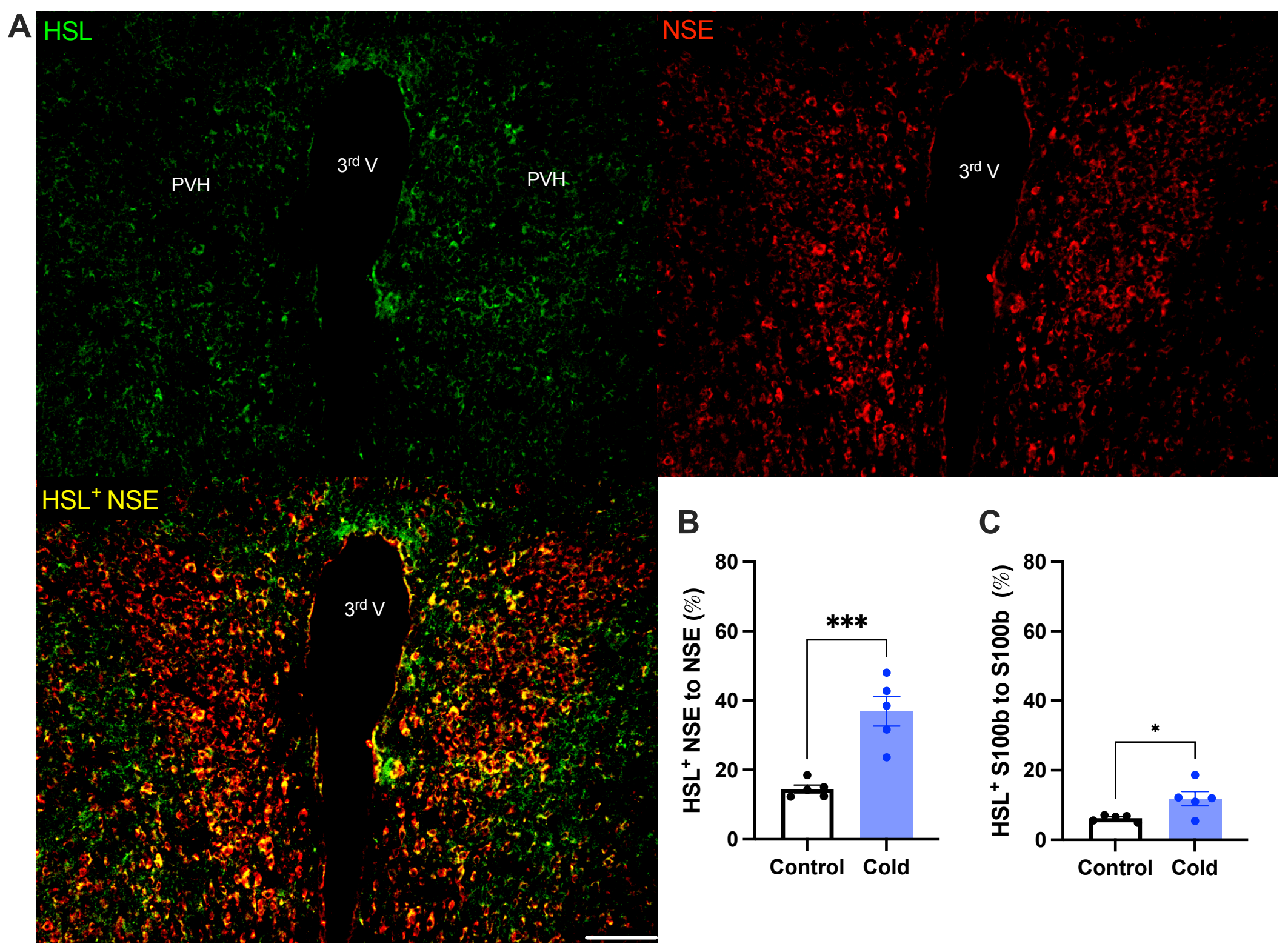
A
HSL
PVH
3rd V
PVH
NSE
3rd V
HSL+ NSE
3rd V
B
HSL+ NSE to NSE (%)
80
60
40
20
0
***
Control
Cold
C
HSL+ S100b to S100b (%)
80
60
40
20
0
*
Control
Cold

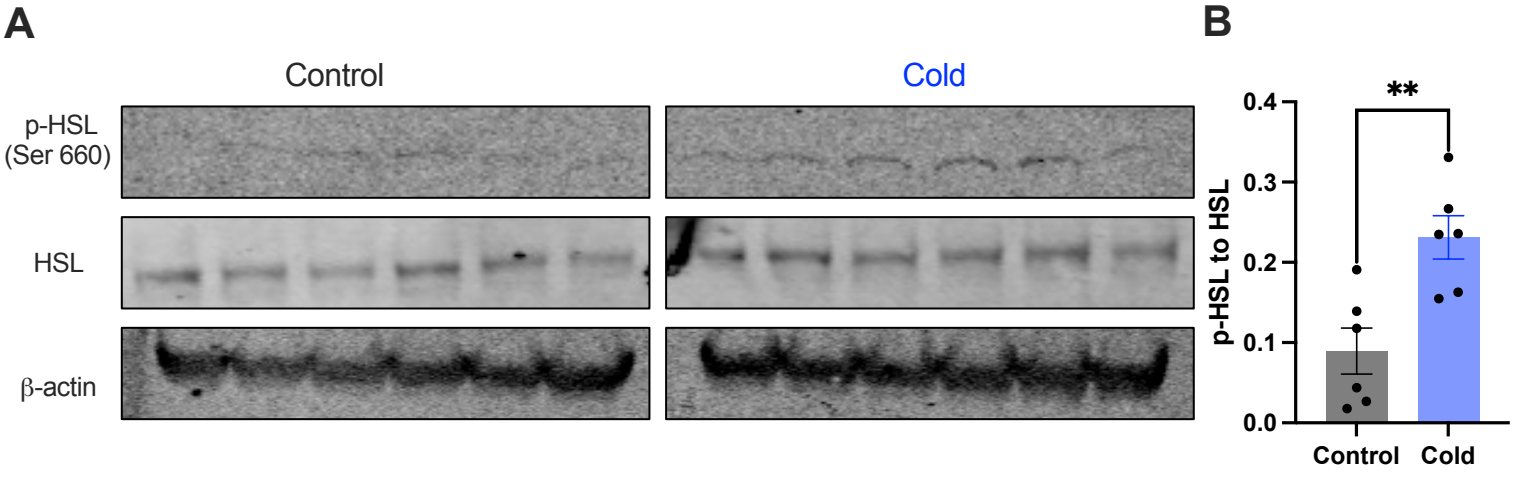
A
Control
Cold
p-HSL
(Ser 660)
HSL
β-actin
B
**
p-HSL to HSL
0.4
0.3
0.2
0.1
0.0
Control
Cold

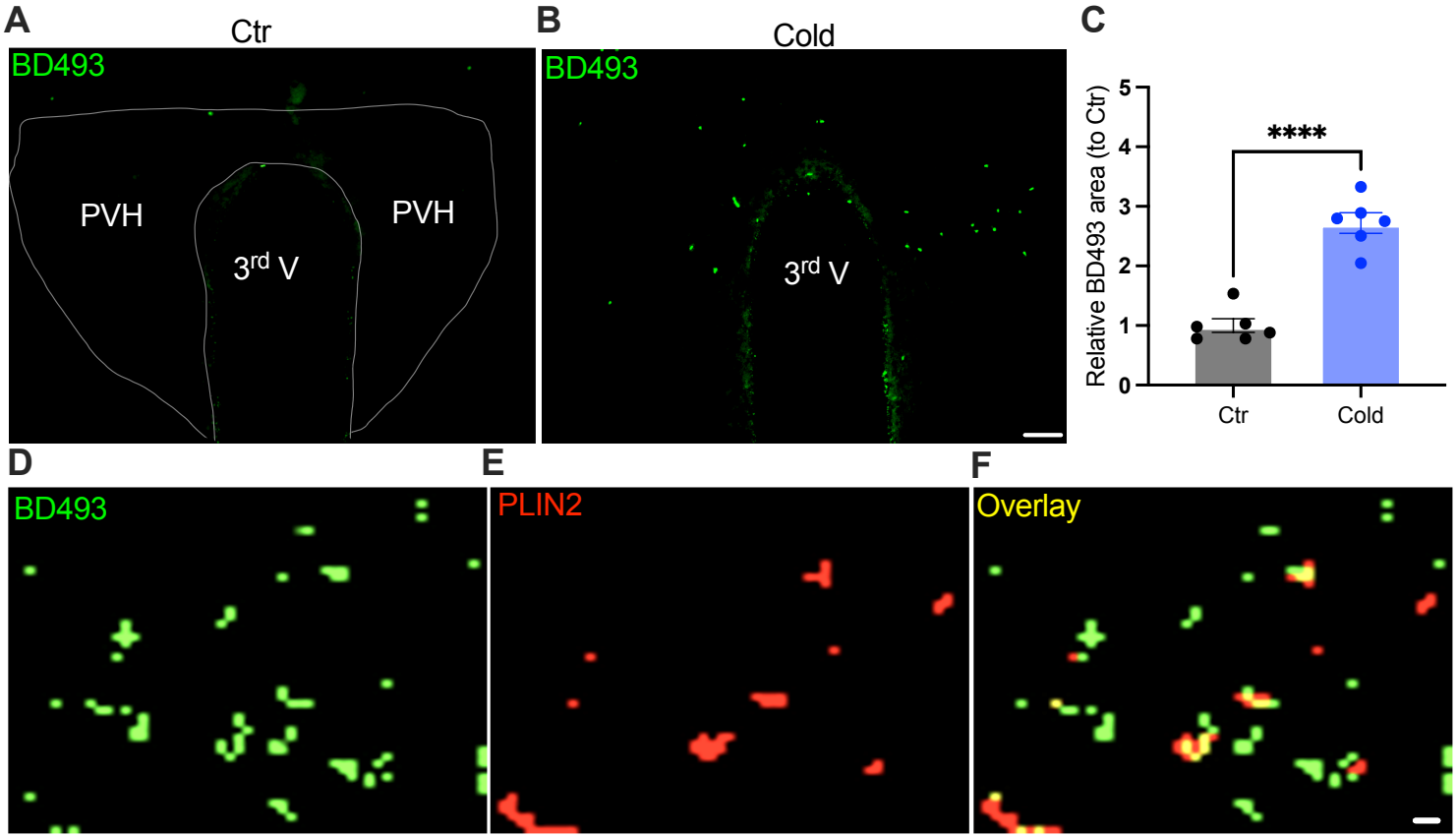
A
Ctr
BD493
PVH
PVH
3rd V
B
Cold
BD493
3rd V
C
Relative BD493 area (to Ctr)
0
1
2
3
4
5
****
Ctr
Cold
D
BD493
E
PLIN2
F
Overlay

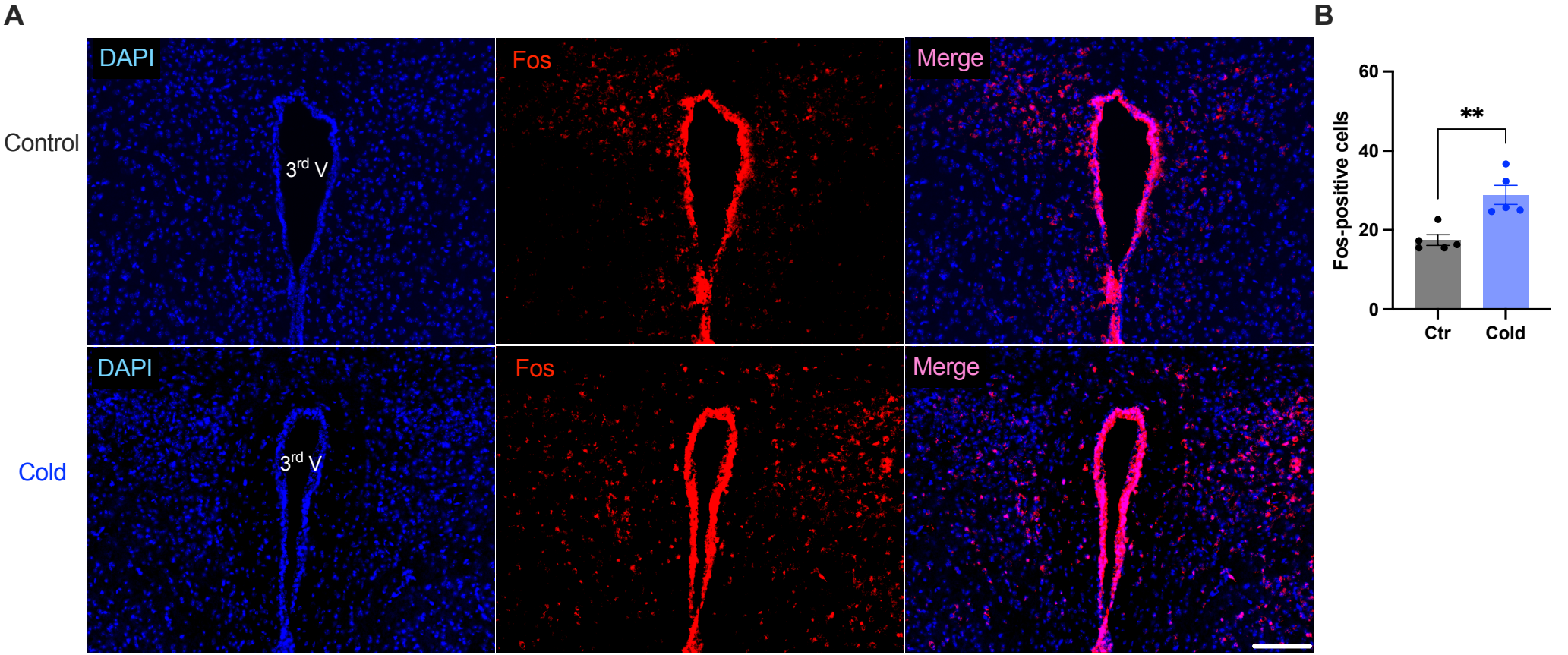
A
B
DAPI
Fos
Merge
Control
Cold
3rd V
Fos-positive cells
60
40
20
0
**
Ctr
Cold

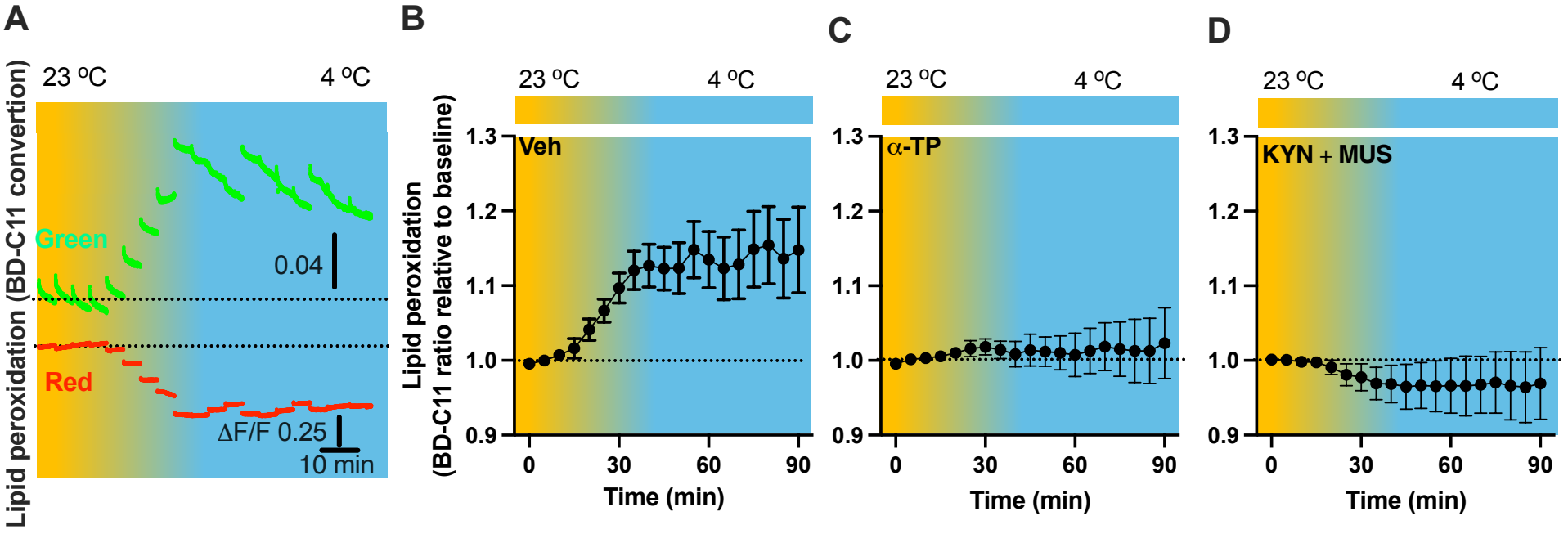
A
23 ºC
4 ºC
Lipid peroxidation (BD-C11 convertion)
Green
0.04
Red
ΔF/F 0.25
10 min
B
23 ºC
4 ºC
Lipid peroxidation
(BD-C11 ratio relative to baseline)
Veh
1.3
1.2
1.1
1.0
0.9
0
30
60
90
Time (min)
C
23 ºC
4 ºC
α-TP
1.3
1.2
1.1
1.0
0.9
0
30
60
90
Time (min)
D
23 ºC
4 ºC
KYN + MUS
1.3
1.2
1.1
1.0
0.9
0
30
60
90
Time (min)

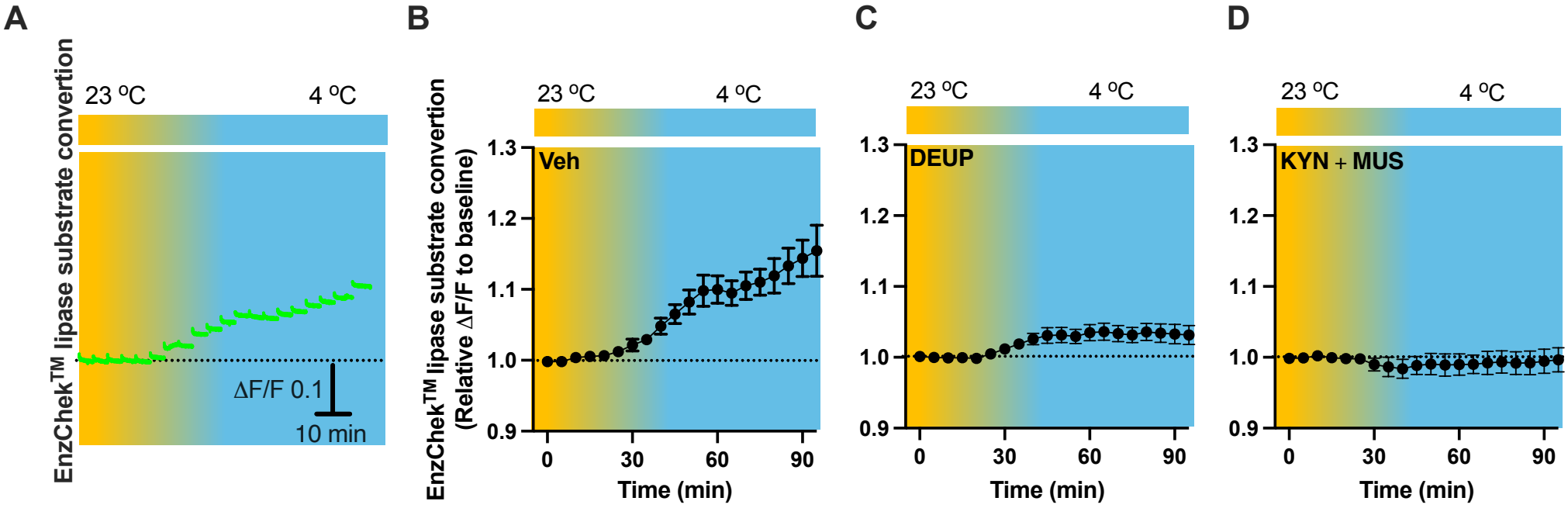
A
B
C
D
23 °C
4 °C
EnzChek™ lipase substrate convertion
ΔF/F 0.1
10 min
EnzChek™ lipase substrate convertion
(Relative ΔF/F to baseline)
Veh
DEUP
KYN + MUS
1.3
1.2
1.1
1.0
0.9
0
30
60
90
Time (min)

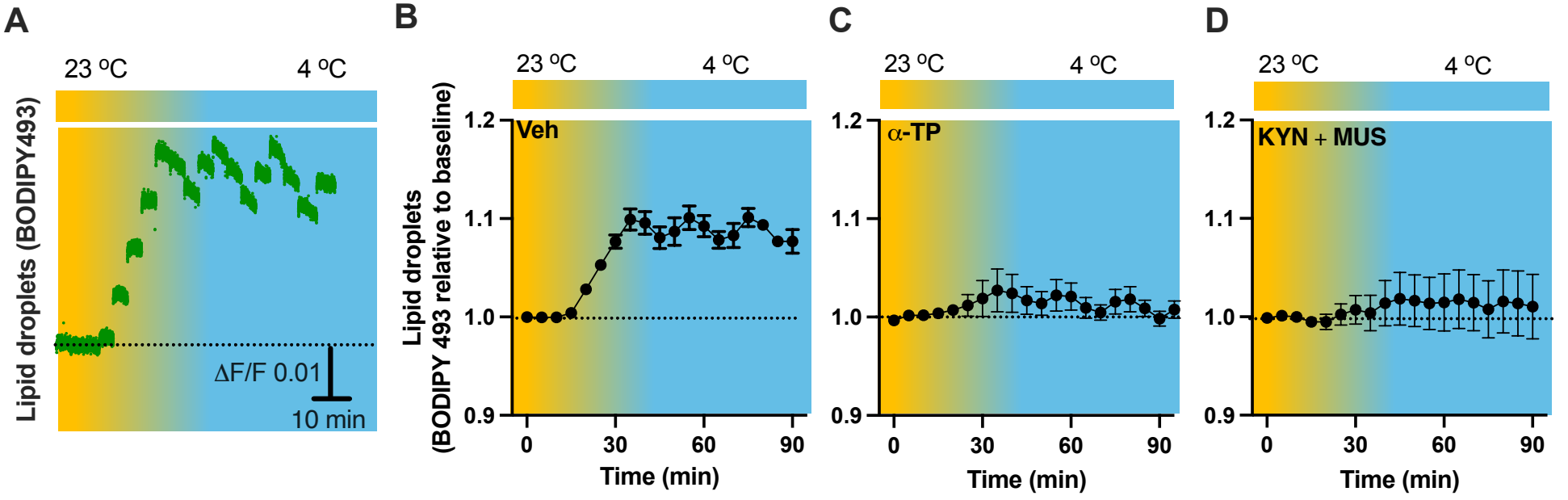
A
23 ºC
4 ºC
Lipid droplets (BODIPY493)
ΔF/F 0.01
10 min
B
23 ºC
4 ºC
Veh
Lipid droplets
(BODIPY 493 relative to baseline)
1.2
1.1
1.0
0.9
0
30
60
90
Time (min)
C
23 ºC
4 ºC
α-TP
1.2
1.1
1.0
0.9
0
30
60
90
Time (min)
D
23 ºC
4 ºC
KYN + MUS
1.2
1.1
1.0
0.9
0
30
60
90
Time (min)